Monthly Notices
of the
ROYAL ASTRONOMICAL SOCIETY

MNRAS **437,** 2831–2844 (2014)
Advance Access publication 2013 November 26

doi:10.1093/mnras/stt2100

The mass–radius relationship for very low mass stars: four new discoveries from the HATSouth Survey*

G. Zhou,[1]† D. Bayliss,[1] J. D. Hartman,[2,3] G. Á. Bakos,[2,3]‡§ K. Penev,[2,3] Z. Csubry,[2,3] T. G. Tan,[4] A. Jordán,[5] L. Mancini,[6] M. Rabus,[5] R. Brahm,[5] N. Espinoza,[5] M. Mohler-Fischer,[6] S. Ciceri,[6] V. Suc,[5] B. Csák,[6] T. Henning[6] and B. Schmidt[1]

[1]*Research School of Astronomy and Astrophysics, Australian National University, Canberra, ACT 2611, Australia*
[2]*Department of Astrophysical Sciences, Princeton University, NJ 08544, USA*
[3]*Harvard–Smithsonian Center for Astrophysics, Cambridge, MA 02138, USA*
[4]*Perth Exoplanet Survey Telescope, Perth, Australia*
[5]*Instituto de Astrofísica, Pontificia Universidad Católica de Chile, Av. Vicuña Mackenna 4860, 7820436 Macul, Santiago, Chile*
[6]*Max Planck Institute for Astronomy, Königstuhl 17, D-69117 Heidelberg, Germany*

Accepted 2013 October 27. Received 2013 October 24; in original form 2013 October 4

ABSTRACT

We report the discovery of four transiting F-M binary systems with companions between 0.1 and 0.2 $M_\odot$ in mass by the HATSouth survey. These systems have been characterized via a global analysis of the HATSouth discovery data, combined with high-resolution radial velocities and accurate transit photometry observations. We determined the masses and radii of the component stars using a combination of two methods: isochrone fitting of spectroscopic primary star parameters and equating spectroscopic primary star rotation velocity with spin–orbit synchronization. These new very low mass companions are HATS550-016B ($0.110^{+0.005}_{-0.006}\,M_\odot$, $0.147^{+0.003}_{-0.004}\,R_\odot$), HATS551-019B ($0.17^{+0.01}_{-0.01}\,M_\odot$, $0.18^{+0.01}_{-0.01}\,R_\odot$), HATS551-021B ($0.132^{+0.014}_{-0.005}\,M_\odot$, $0.154^{+0.006}_{-0.008}\,R_\odot$) and HATS553-001B ($0.20^{+0.01}_{-0.02}\,M_\odot$, $0.22^{+0.01}_{-0.01}\,R_\odot$). We examine our sample in the context of the radius anomaly for fully convective low-mass stars. Combining our sample with the 13 other well-studied very low mass stars, we find a tentative 5 per cent systematic deviation between the measured radii and theoretical isochrone models.

Key words: binaries: eclipsing – stars: low-mass.

1 INTRODUCTION

'Very low mass stars' (VLMSs), with masses between 0.08 and 0.3 $M_\odot$, are the most dominant subset of the stellar population (e.g. Kroupa 2001). These stars are thought to have fully convective interiors and hydrogen fusion in their cores, distinguishing them from higher mass stars and brown dwarfs, respectively (see review by Chabrier & Baraffe 2000). Mass and radius are two of the most fundamental measurements for stars. Previous studies have shown that the radii of subsolar mass stars are underpredicted by theoretical interior models at the 5–10 per cent level (e.g. Torres & Ribas 2002; Ribas 2006; Torres, Andersen & Giménez 2010; Feiden & Chaboyer 2012; Spada et al. 2013). The interior structure of the fully convective VLMSs is different from that of higher mass, partially radiative stars, and therefore, warrants a more thorough, independent examination.

The vast majority of masses and radii come from dynamical measurements of binary systems. One explanation for the radius anomaly is that when these M-dwarf binaries are spun-up by tidal interactions, the speed-up of the internal dynamo then leads to increased magnetic activities, suppressing convection and increasing star-spot activity (e.g. López-Morales & Ribas 2005; Ribas

* The HATSouth network is operated by a collaboration consisting of Princeton University (PU), the Max Planck Institute für Astronomie (MPIA) and the Australian National University (ANU). The station at Las Campanas Observatory (LCO) of the Carnegie Institute is operated by PU in conjunction with collaborators at the Pontificia Universidad Católica de Chile (PUC), the station at the High Energy Spectroscopic Survey (HESS) site is operated in conjunction with MPIA and the station at Siding Spring Observatory (SSO) is operated jointly with ANU.

† E-mail: george.zhou@anu.edu.au

‡ Alfred P. Sloan Research Fellow.
§ Packard Fellow.

2006; López-Morales 2007; Morales et al. 2010). Chabrier, Gallardo & Baraffe (2007) showed that the general radius discrepancies for low-mass stars can be accounted for by allowing large spot coverages and varied mixing length in the models. However, since the magnetic field is thought to be generated differently in fully convective stars (e.g. Chabrier & Küker 2006), the effect of this spin-up on the VLMSs and the resulting spot coverage is unclear. In addition, the effect of the mixing length parameter incorporated in stellar models for fully convective, near adiabatic, stars is significantly less than that for higher mass stars. Any explanation for the radius anomaly should also not be restricted to binaries, since the radius inflation is also observed for isolated M-dwarfs measured via interferometry (e.g. Berger et al. 2006; Boyajian et al. 2012; Spada et al. 2013).

It remains difficult to test stellar models for the VLMS population, given that metallicities and precise (better than 10 per cent) mass radius measurements are available for only 13 previous objects (see Section 4.5). In contrast, we know the masses and radii of ∼40 exoplanets to better than 5 per cent precision, which has led to more thorough examinations of planet interior models (e.g. Laughlin, Crismani & Adams 2011; Swift et al. 2012). The radii of standalone, close-by M-dwarfs can be measured via interferometry (e.g. Ségransan et al. 2003), but the masses must be inferred from empirical mass–luminosity relationships. Dynamical masses of binaries can be obtained via astrometric orbit measurements (e.g. Simon et al. 2013). Double-lined M-M eclipsing binary systems provide accurate, model-independent mass and radius measurements (Metcalfe et al. 1996; Carter et al. 2011; Doyle et al. 2011; Irwin et al. 2011; Nefs et al. 2013), but these systems are relatively rare. In addition, the accuracy of M-M binary-derived system parameters may suffer from M-dwarf activity and unaccounted spot variability, and may not be as reliable as previously thought (Feiden & Chaboyer 2012).

Photometric transit surveys have led to a rapid expansion in the population of transiting exoplanets. VLMSs have radii comparable to that of gas-giant planets and are often found as companions in binary systems to solar-type stars. These F-M binaries exhibit similar transit signals as hot-Jupiter systems and can be easily identified by transiting planet surveys. The population of well-characterized VLMSs can be greatly extended by including single-lined F-M binaries (e.g. Pont et al. 2005, 2006; Beatty et al. 2007; Fernandez et al. 2009; Triaud et al. 2013).

There are a number of approaches towards measuring the mass and radius of M-dwarf companions in single-lined F-M binary systems. The primary star properties can be obtained by combining spectroscopic analysis with stellar evolution models. The precision of the measured companion mass and radius is limited by the uncertainty in the primary star properties. For orbital companions of substantial mass, the rotation of the primary star is quickly synchronized with the companion orbital period. Fundamental system parameters derived from transit light curves, combined with rotational velocities measured from spectra, can yield relatively model-independent masses and radii for both components of a binary system (e.g. Beatty et al. 2007; Fernandez et al. 2009).

In this study, we present the discovery of four single-lined stellar systems with 0.1–0.2 $M_{\odot}$ VLMS companions. These low-mass eclipsing binaries were identified by the HATSouth survey (Bakos et al. 2013). The discovery and follow-up observations are detailed in Section 2. Analysis of the individual systems, including spectral classifications of the primary star, global modelling of the light curves and radial velocity data and descriptions of the methods used to derive the mass and radius of the companions, can be found in Section 3. Section 4 discusses these new discoveries in the context of existing VLMS systems and examines the mass–radius anomaly in the VLMS regime.

2 OBSERVATIONS

2.1 HATSouth photometric detection

The transiting VLMS systems were identified from photometric observations by the HATSouth global network. HATSouth consists of six telescope units spread over three sites, SSO in Australia, LCO in Chile and the HESS site in Namibia, providing continuous monitoring of 128 $\deg^2$ fields in the southern sky (Bakos et al. 2013). Each unit consists of four 0.18 m *f*/2.8 Takahasi astrographs and Apogee Alta-U16M D9 4 K × 4 K front illuminated CCD cameras, with 9 μm pixels, and a plate scale of 3.7 arcsec pixel^{-1}. The four telescopes are offset by 4°, allowing four adjacent 4° × 4° fields to be simultaneously monitored. The observations are made at 4 min cadence in the r' band. Each field is monitored for ∼2 months by a unit at each HATSouth station. Aperture photometry is performed on the reduced frames and detrended using external parameter decorrelation (Bakos et al. 2007) and the trend filtering algorithm (TFA; Kovács, Bakos & Noyes 2005). Objects exhibiting periodic transit signals are identified using the Box-fitting Least-Squares technique (Kovács, Zucker & Mazeh 2002).

The HATSouth discovery light curves for the systems presented in this study are shown in Fig. 1 and are summarized in Table 1. Details of our planetary candidate selection, vetting and confirmation process can be found in the recent HATSouth publications (Bayliss et al. 2013; Mohler-Fischer et al. 2013; Penev et al. 2013).

2.2 Identification of stellar mass binaries by ANU 2.3 m/WiFeS

Spectroscopic follow-up of HATSouth candidates starts with reconnaissance spectroscopic observations, at high signal-to-noise (S/N) and low–medium resolution, to determine preliminary primary star properties and to search for high-amplitude radial velocity variations ($>2\,\mathrm{km\,s^{-1}}$). These observations allow efficient identification of non-planetary systems, such as F-M binaries, by providing an initial mass estimate for the primary star and any secondary companion found. The reconnaissance observations are summarized in Table 2.

Initial spectroscopic observations of the targets were obtained using the Wide Field Spectrograph (WiFeS) on the ANU 2.3 m telescope (Dopita et al. 2007), located at SSO, Australia.

First, a low-resolution ($R \equiv \lambda/\Delta\lambda = 3000$) spectrum covering the wavelength region 3500–6000 Å was used to obtain an initial stellar classification of the target star. The flux calibrated spectrum was fitted to a grid of synthetic spectra from Gustafsson et al. (2008). The details of the low-resolution spectral reduction and analysis, including fitting of the stellar properties, are given in Bayliss et al. (2013). These stellar parameters are later refined using high-resolution spectra (see Section 3.1).

Subsequent medium resolution, multi-epoch radial velocity observations were performed with WiFeS at $R = 7000$, observed at phase quadratures of the photometric ephemeris, where the potential velocity variation is greatest. In the case of stellar binaries, the radial velocity variations are often apparent with two well-time exposures. Combined with the WiFeS stellar parameters, the WiFeS radial velocity orbit provides an initial mass estimate of the companions and affects their prioritization for further follow-up studies. The WiFeS velocities were not included in the final system

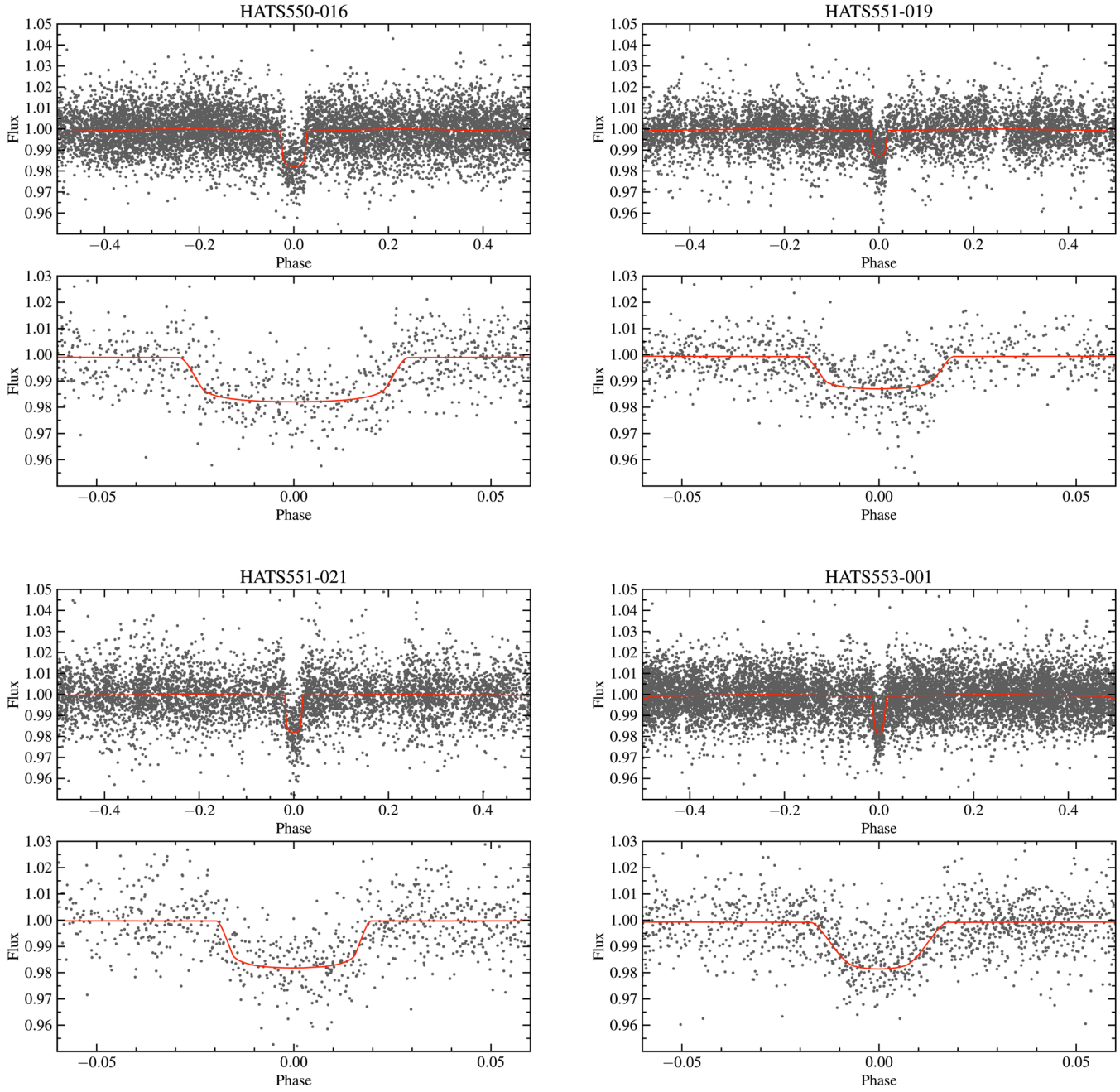

Figure 1. HATSouth discovery light curves of the four VLMS systems, including close-ups of the transit event. The best-fitting models from Section 3.2 are plotted in red.

analysis, since fewer lower resolution observations do not contribute greatly to improving the precision of the measured radial velocity orbit.

2.3 High-resolution spectroscopic follow-up

Radial velocity measurements derived from high-resolution spectroscopic observations were obtained for the VLMS systems using the Echelle spectrograph on the ANU 2.3 m telescope at SSO, the fibre-fed echelle spectrograph CORALIE on the Swiss Leonard Euler 1.2 m telescope (Queloz et al. 2000) at La Silla Observatory (LSO), Chile, and the fibre-fed echelle spectrograph FEROS on the MPG/ESO 2.2 m telescope (Kaufer & Pasquini 1998) at LSO. The observations are summarized in Table 2. Descriptions of the data reduction and analysis for CORALIE and FEROS can be found in Penev et al. (2013, also see Jordán et al. in preparation). This is the first time we have used the ANU 2.3 m Echelle to monitor HATSouth targets; a description of these observations is presented below. The observations are listed in Table 1, with the radial velocities plotted in Figs 1–4.

2.3.1 ANU 2.3 m/Echelle

High-resolution spectra of the systems were obtained using the Echelle spectrograph on the ANU 2.3 m telescope. The Echelle was configured to a 1.8 arcsec wide slit, delivering a resolution of $R = 24\,000$ and velocity dispersion of 4.0 km s^{-1} pixel^{-1}, in the

Table 1. Summary of photometric observations.

Facility	Date(s)	Filter	Number of images	Cadence (s)
HATS550-016				
HATSouth	2009/09/28–2010/12/20	r'	8726	240
FTS/Merope	2012/11/17	i'	160	60
MPG/ESO 2.2 m/GROND	2012/12/08	g', i', z'	187	145
MPG/ESO 2.2 m/GROND	2012/12/08	r'	185	145
HATS551-019				
HATSouth	2009/09/09–2010/04/29	r'	5274	240
PEST	2012/12/23	R_c	168	120
HATS551-021				
HATSouth	2009/09/09–2010/04/29	r'	5274	240
HATS553-001				
HATSouth	2009/09/17–2010/09/10	r'	10703	240
PEST	2012/12/22	R_c	92	120

Table 2. Summary of spectroscopic observations.

Facility	Date range	Resolution	Wavelength coverage (Å)	Number of observations
HATS550-016				
ANU 2.3 m/WiFeS	2012/05/11–2012/08/07	3000	3500–6000	2
ANU 2.3 m/WiFeS	2012/08/04–2012/10/31	7000	5200–7000	16
Euler 1.2 m/CORALIE	2012/08/25–2012/11/11	60 000	3850–6900	7
ANU 2.3 m/Echelle	2012/12/04–2012/12/06	24 000	4200–6725	7
HATS551-019				
Euler 1.2 m/CORALIE	2010/10/28–2011/02/18	60 000	3850–6900	3
ANU 2.3 m/WiFeS	2010/11/26–2011/04/19	7000	5200–7000	4
ANU 2.3 m/Echelle	2013/03/23–2013/04/01	24 000	4200–6725	7
HATS551-021				
Euler 1.2 m/CORALIE	2010/10/28-2011/02/18	60 000	3850–6900	3
ANU 2.3 m/WiFeS	2010/11/26–2011/09/17	7000	5200–7000	3
MPG/ESO 2.2 m/FEROS	2011/09/09-2011/09/10	48 000	3500–9200	2
ANU 2.3 m/WiFeS	2011/09/17	3000	3500–6000	1
ANU 2.3 m/Echelle	2013/03/23–2013/04/01	24 000	4200–6725	7
HATS553-001				
ANU 2.3 m/WiFeS	2012/05/08	3000	3500–6000	1
ANU 2.3 m/WiFeS	2012/05/09–2012/05/09	7000	5200–7000	2
ANU 2.3 m/Echelle	2013/03/23–2013/04/01	24 000	4200–6725	7

spectral range 4200–6725 Å, over 20 echelle orders. The detector is a $2\,\mathrm{K} \times 2\,\mathrm{K}$ CCD with a gain of $2\,e^-\,\mathrm{ADU}^{-1}$ and read noise of $2.3\,\mathrm{ADU\,pixel}^{-1}$, and binned two times in the spatial direction. A number of instrument limitations prevent us from achieving better than $500\,\mathrm{m\,s}^{-1}$ velocity precision. For example, the instrument is mounted on the Nasmyth focus, not in a temperature stabilized environment; the low efficiency of the spectrograph limits the study to only bright stars ($<13.5\,V_{\mathrm{mag}}$). The data were reduced with the IRAF[1] package CCDPROC and extracted using ECHELLE. A rapidly rotating B-star spectrum is divided through each observation to remove the blaze function. A low-order spline interpolation is then used to continuum normalize each spectrum. The wavelength solution was provided by ThAr arc lamp exposures that bracketed each science exposure.

[1] IRAF is distributed by the National Optical Astronomy Observatories, which are operated by the Association of Universities for Research in Astronomy, Inc., under cooperative agreement with the National Science Foundation.

Radial velocity measurements were obtained by cross-correlating the object spectra against a series of radial velocity standard star spectra taken on the same night. The radial velocities derived from selected echelle orders not severely contaminated by telluric absorption features were sigma clipped and weight averaged according to their respective cross correlation function (CCF) heights and S/Ns. Typically, 15 echelle orders were used in the cross-correlations. A velocity and the associated uncertainty were determined for each order, from which the weighted average and standard deviation were calculated and adopted as the measured velocity. For stable HATSouth candidates with $V_{\mathrm{mag}} \approx 13$, the long-term root-mean-squared (rms) velocity scatter of the instrument is $\sim 1.0\,\mathrm{km\,s}^{-1}$. Stellar parameters were also derived from the Echelle spectra; the process is described in detail in Section 3.1.

2.4 Photometric follow-up

Follow-up photometric confirmations for the transit events of HATS550-016B, HATS551-019B, and HATS553-001B were made

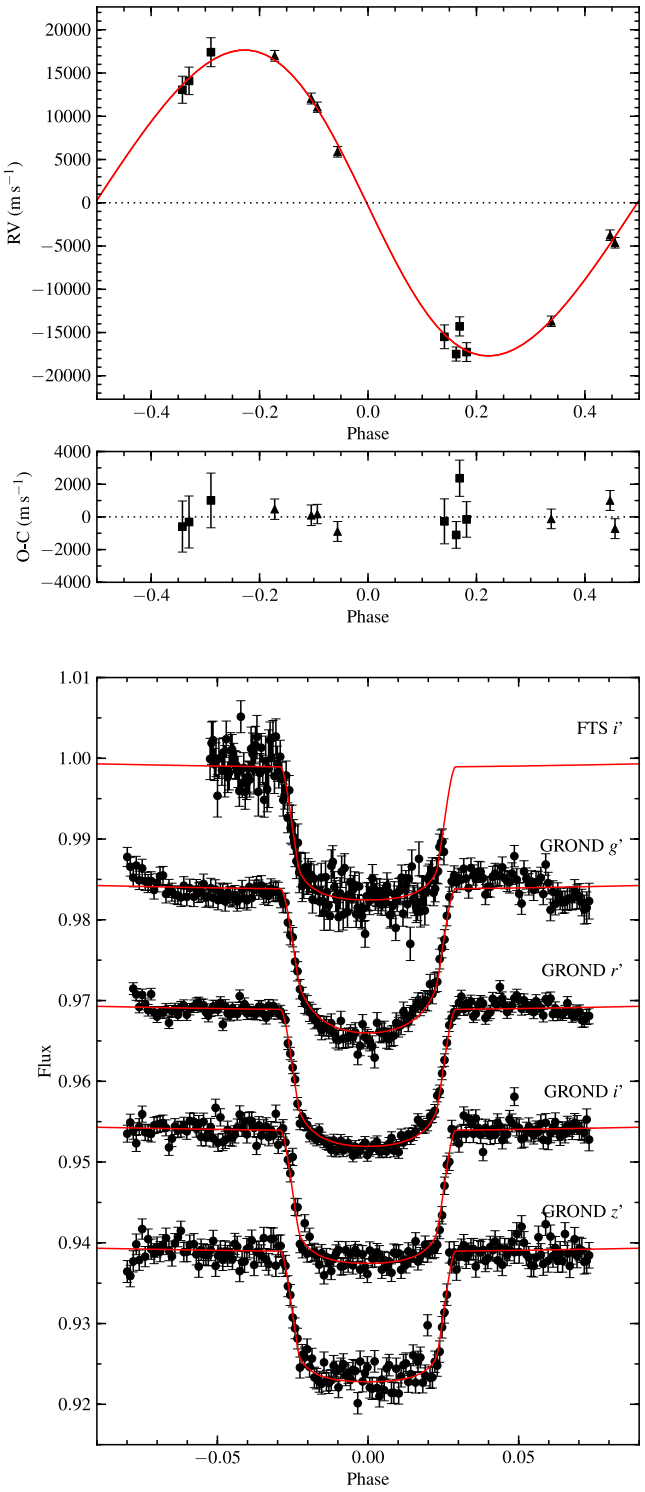

Figure 2. Top: HATS550-016 radial velocities and the Keplerian orbit fit. ANU 2.3 m Echelle data are plotted as squares, and CORALIE data as triangles. Bottom: follow-up transit light curve and model fit.

using the Merope camera on the 2 m Faulkes Telescope South (FTS) located at SSO, the Gamma-Ray Burst Optical/Near-Infrared Detector (GROND) on the MPG/ESO 2.2 m telescope at LSO and the 0.30 m Perth Exoplanet Survey Telescope (PEST) located in Perth, Australia. The observations are listed in Table 1, with the light curves plotted in Figs 2, 3 and 5.

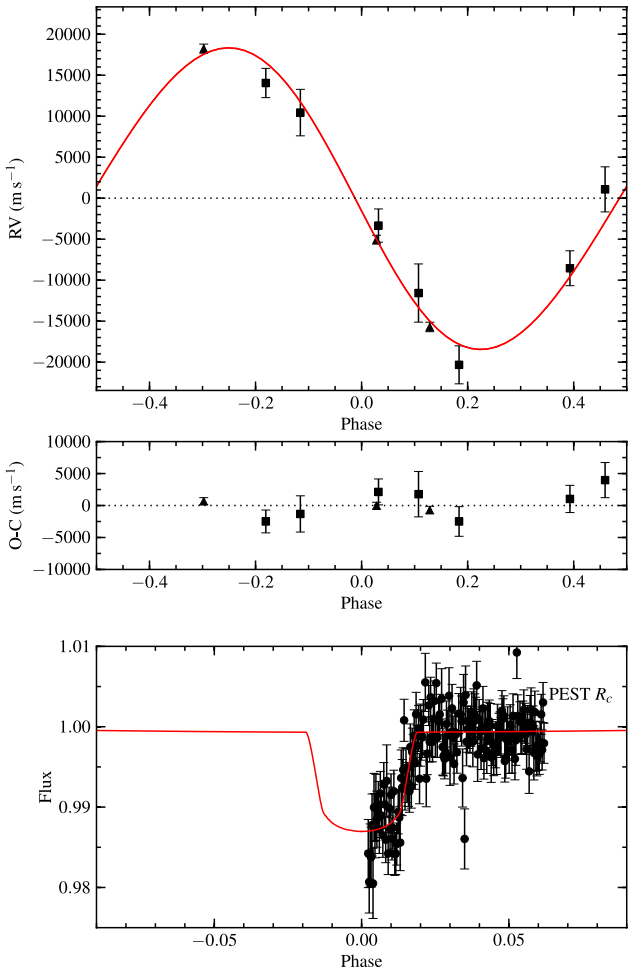

Figure 3. Top: HATS551-019 radial velocities and the Keplerian orbit fit. ANU 2.3 m Echelle data are plotted as squares, and CORALIE data as triangles. Bottom: follow-up transit light curve and model fit.

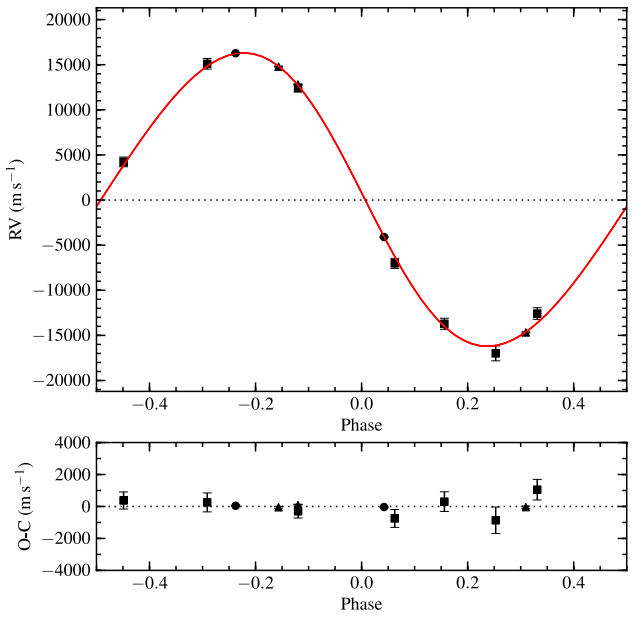

Figure 4. HATS551-021 radial velocities and the Keplerian orbit fit. ANU 2.3 m Echelle data are plotted as squares, CORALIE data as triangles and FEROS data as circles.

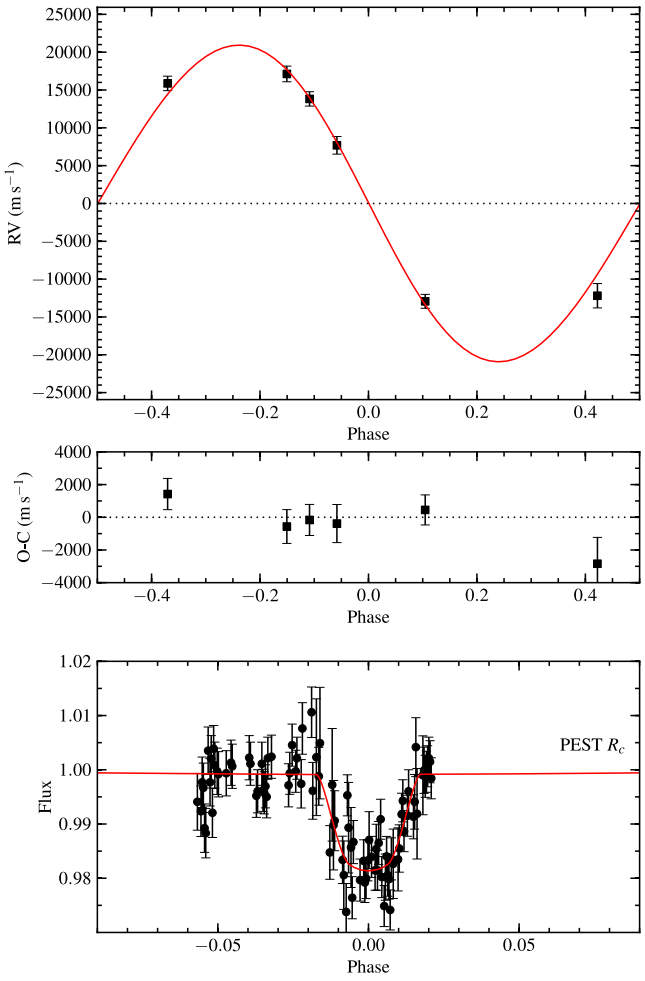

Figure 5. Top: HATS553-001 radial velocities and the Keplerian orbit fit. ANU 2.3 m Echelle data are plotted as squares. Bottom: follow-up transit light curve and model fit.

2.4.1 *FTS 2 m/Merope*

A near-full transit for HATS550-016B was observed on 2012 November 17 using the Merope imaging camera on the 2 m FTS, part of the Las Cumbres Global Telescope (LCOGT) Network. Merope is a 2 K × 2 K camera with 0.139 arcsec pixel^{-1} pixels, binned at 2 × 2, and a field of view (FoV) of 4.7 arcmin × 4.7 arcmin. The observation was performed in the SDSS i' band, with 60 s exposure time, and the telescope slightly defocused to reduce pixel–pixel and imperfect flat-field systematic effects and to prevent saturation. The data were reduced by the automated LCOGT pipeline.

Aperture photometry was performed on the reduced images with Source Extractor (Bertin & Arnouts 1996). Stellar flux was extracted over multiple diameter apertures, and reference stars were selected based on their brightness, colour and lack of blended neighbours.

2.4.2 *MPG/ESO 2.2 m/GROND*

A full transit for HATS550-016B was also observed on 2012 December 08 using GROND on the 2.2 m MPG/ESO telescope at LSO. GROND provides simultaneous multiband photometry in four optical bands similar to Sloan g', r', i' and z'. It has an FoV of 5.4 arcmin × 5.4 arcmin with 0.158 arcsec pixel^{-1} pixels. The exposure time for the HATS550-016 observations was 100 s. Details of the GROND observing strategy and data reduction procedure can be found in Penev et al. (2013) and Mohler-Fischer et al. (2013).

2.4.3 *PEST*

A full transit of HATS553-001 and a partial transit of HATS551-019 were observed using PEST on 2012 December 22 and 23, respectively. PEST is a fully automated 0.30 m Meade LX200 Schmidt Cassegrain telescope located at latitude −31° 59′ 34″ and longitude 115° 47′ 53″E. The telescope is coupled with a focal reducer to yield a focal ratio of *f*/5. The detector is an SBIG ST-8XME CCD camera with a gain of 2.27 e^- ADU^{-1} and read noise of 19.9 e^-, and with image scale of 1.2 arcsec pixel^{-1}, and an FoV of 31 arcmin × 21 arcmin. Images were taken in the R_c band, with the telescope in focus; exposure times are provided in Table 1. Typical conditions yield stellar point spread functions with full width at half-maximum ∼3 pixels. Flat-field frames were taken in twilight whenever possible. Dark frames of equal exposure length to the object frames were drawn from a library of master dark frames, renewed every month.

Image reduction and aperture photometry were performed using the C-Munipack program. Relative photometry is performed, with the reference light curve made from the weighted average of high S/N field star light curves.

3 ANALYSIS

3.1 Fundamental stellar atmospheric parameters

The fundamental primary star properties, including effective temperature ($T_{\rm eff}$), surface gravity ($\log g$), metallicity ([Fe/H]) and projected rotational velocity ($v \sin i_{\rm rot}$), were derived by fitting synthetic model spectra to the averaged ANU 2.3 m/Echelle observations. We generated a synthetic spectral library with the ATLAS9 model atmospheres (Castelli & Kurucz 2004), using the spectral synthesis program SPECTRUM[2] (Gray & Corbally 1994). The spectra have resolutions of $R = 24\,000$, matching that of the Echelle instrument; they were generated at the ATLAS9 $T_{\rm eff}$, $\log g$ and [Fe/H] grid points, using the default isotopic line lists provided with SPECTRUM, and then broadened to multiple rotational velocities spaced 5 km s^{-1} apart. Model microturbulences are fixed at 2 km s^{-1}, given that the range of possible microturbulence values for the $T_{\rm eff}$ and $\log g$ tested varies only by ∼0.5 km s^{-1} (Husser et al. 2013). The individual echelle orders of the observed spectrum were matched to a restricted grid, centred about the rough stellar parameter estimates from the WiFeS spectrum. Using exposures of standard stars, we found echelle orders that gave the most reliable stellar parameters for a target of a given spectral type. The fitting results from these selected orders were weight averaged according to their rms scatter from the fit. The $\log g$ was subsequently constrained from theoretical isochrones (see Section 3.2) via global light curve and radial velocity modelling. We then performed the grid search again, at a finer $v \sin i_{\rm rot}$ grid of 1 km s^{-1} spacings, with $\log g$ fixed, to obtain the final stellar parameters. The primary star parameters are presented in Table 3.

To investigate the errors in our spectral typing pipeline, we observed seven reference stars from Valenti & Fischer (2005), and four known planet hosting stars of similar spectral type and brightness to our candidates (WASP-61, 62, 78 and 79; Hellier et al. 2012; Smalley et al. 2012). These observations were used to determine

[2] http://www1.appstate.edu/dept/physics/spectrum/spectrum.html

Table 3. Primary star properties.

Property	HATS550-016	HATS551-019	HATS551-021	HATS553-001
GSC[a]	6465-00602	6493-00290	6493-00315	5946-00892
RA[b] (J2000 HH:MM:SS.SS)	04:48:23.32	05:40:46.16	05:42:49.12	06:16:00.66
DEC[b] (J2000 DD:MM:SS.SS)	−24:50:16.88	−24:55:35.16	−25:59:47.49	−21:15:23.82
Photometric properties				
V[c]	13.605 ± 0.041	12.058 ± 0.006	13.114 ± 0.008	13.189 ± 0.021
B[c]	14.052 ± 0.020	12.497	13.580 ± 0.012	13.694 ± 0.014
g'[c]	13.782 ± 0.032	12.198	13.308	13.408
r'[c]	13.499 ± 0.031	11.953	13.044	13.102
i'[c]	13.438	11.922 ± 0.038	12.985 ± 0.077	13.988
J[b]	12.640 ± 0.021	11.146 ± 0.021	12.150 ± 0.021	12.245 ± 0.021
H[b]	12.379 ± 0.025	10.943 ± 0.024	11.956 ± 0.020	12.023 ± 0.025
K[b]	12.308 ± 0.021	10.914 ± 0.021	11.873 ± 0.023	11.970 ± 0.024
Derived spectroscopic properties				
$T_{\rm eff}$ (K)	6420 ± 90	6380 ± 170	6670 ± 220	6230 ± 250
[Fe/H]	−0.60 ± 0.06	−0.4 ± 0.1	−0.4 ± 0.1	−0.1 ± 0.2
$v \sin i_{\rm rot}$ (km s^{-1})	30.0 ± 1.7	17.1 ± 2.0	16.4 ± 10.6	22.2 ± 1.8

[a]Hubble guide star catalogue.
[b]2MASS.
[c]APASS Data Release 7, uncertainties are quoted where available as the scatter from multiple observations.

the echelle orders that yielded the most reliable spectral types. Reference stars with $v \sin i > 10\,{\rm km\,s^{-1}}$ were also analysed at the finer $1\,{\rm km\,s^{-1}}$ $v \sin i_{\rm rot}$ grid spacing. We are not sensitive to rotational velocities of $v \sin i < 10\,{\rm km\,s^{-1}}$, where we become limited by the instrument resolution. The rms differences between our measured stellar parameters and literature values are 113 K in $T_{\rm eff}$, 0.19 dex in $\log g$, 0.12 dex in [Fe/H] and $4.4\,{\rm km\,s^{-1}}$ in $v \sin i_{\rm rot}$. After correcting for an empirical offset in each parameter, we get errors of 88 K in $T_{\rm eff}$, 0.13 dex in $\log g$, 0.09 dex in [Fe/H] and $0.7\,{\rm km\,s^{-1}}$ in $v \sin i_{\rm rot}$. The offsets have been incorporated in the stellar parameters presented here.

Macroturbulence and microturbulence are free parameters in 1D stellar atmosphere models that contribute to the overall broadening of the spectral features. We investigate the degeneracy between these parameters and the measured stellar rotational broadening. The spectrum of HATS550-016 was fitted to synthetic spectral grids generated at macro- and microturbulences from 0 to $5\,{\rm km\,s^{-1}}$, producing a mean variation of $0.8\,{\rm km\,s^{-1}}$ in the resulting $v \sin i_{\rm rot}$ measurement, smaller than our quoted measurement errors. Since the rotational broadening parameter for all host stars studied is much larger than the broadening from macro- and microturbulence, we conclude minimal systematic uncertainty contributions from these parameters. In addition, we checked for the dependence of the measured $v \sin i_{\rm rot}$ to the synthetic spectral resolution and found a variation of $0.6\,{\rm km\,s^{-1}}$ over a change in resolution of 1000. Since the resolution is measured from the ThAr arc lamp spectra, we expect no significant contribution from uncertainties in the resolution to the $v \sin i_{\rm rot}$ systematic uncertainties.

3.2 Global modelling of data

To derive the system properties, we performed simultaneous modelling of the HATSouth discovery photometry, follow-up photometry where available and radial velocity measurements. The light curves were modelled using the Nelson & Davis (1972) model for eclipsing binaries, allowing for ellipsoidal phase variations, as implemented in the JKTEBOP code (Popper & Etzel 1981; Southworth, Maxted & Smalley 2004). The Keplerian orbit was used to model the radial velocity measurements.

The free parameters in the global fit include the orbital period P, transit time T_0, radius ratio R_2/R_1, normalized radius sum $R_{\rm sum} = (R_1 + R_2)/a$, radial velocity orbit semi-amplitude K, eccentricity parameters $e\cos\omega$ and $e\sin\omega$, and inclination i. Quadratic limb darkening coefficients for the primary star were fixed to values as from Claret (2000). We assume uniform priors for all the free parameters. In the cases where the proposed iteration in inclination is $i > 90^\circ$, we adopt the $180^\circ - i$ geometry to avoid the discontinuous boundary. To account for the non-zero flux contribution from the M-dwarf companion, we also obtained an approximate surface brightness estimate for the companion using a 5 Gyr Baraffe et al. (1998) isochrone. However, the flux contribution from the M-dwarf is $\ll$0.1 per cent in the R band and is negligible. Ellipsoidal variations are included in the model by including the mass ratio parameter q, using masses determined per iteration from isochrone fitting (see Section 3.3.1). The best-fitting parameters and the surrounding error space were explored by the *emcee* (Foreman-Mackey et al. 2013) implementation of an Markov chain Monte Carlo (MCMC) ensemble sampler, with the individual measurement errors for all data sets (discovery, follow-up photometry and radial velocity) inflated such that the reduced χ^2 is at unity.

Instrumental offsets were derived for each instrument separately. In addition, the HATSouth discovery light curves can be diluted in eclipse depth if they are treated by the TFA detrending algorithm. In the cases where well-sampled follow-up photometry is available (HATS550-016 and HATS553-001), we fitted for a dilution factor for the HATSouth light curves, using the follow-up light curve as reference. Where follow-up photometry of the full transit is not available (HATS551-019 and HATS551-021), simultaneous TFA corrections were performed on the HATSouth light curve using the transit model for each MCMC iteration (see section 6, Kovács et al. 2005).

3.3 Determination of mass and radius

We derive the mass and radius of the primary and secondary stars at each iteration via (1) determination of the primary star properties from stellar isochrones using measured spectroscopic and light curve parameters, (2) assuming spin–orbit synchronization for

the system and deriving mass and radius from the spectroscopic $v \sin i_{\rm rot}$ measurement, and (3) a combined analysis that includes isochrone fitting and the assumption of spin–orbit synchronization. Each analysis employs a separate MCMC routine that explores their respective posteriors.

3.3.1 Isochrone fitting

Sozzetti et al. (2007) showed that the normalized orbital distance a/R_1, derived from the global fit, can be combined with model isochrones to refine the stellar atmosphere parameters. a/R_1 is related to the mean stellar density by

$$\frac{M_1}{R_1^3} = \frac{4\pi^2}{GP^2}\left(\frac{a}{R_1}\right)^3 - \frac{M_2}{R_1^3}. \quad (1)$$

Although the second term is usually insignificant and often discarded in the case of transiting planets, it cannot be ignored for stellar mass companions (Triaud et al. 2013). Therefore, for each iteration of the minimization and MCMC routines, we used initial estimates of M_1 and R_1 to derive M_2 from the radial velocity orbit, then used the M_2 estimate and the fitted a/R_1 and spectroscopically determined $T_{\rm eff}$ and [Fe/H] to derive new theoretical M_1 and R_1 values by isochrone fitting. Finally, the new primary mass and radius were used to derive a refined M_2 estimate. The Yonsei-Yale isochrones (Yi et al. 2001) provide the theoretical stellar masses and radii. To incorporate the uncertainties in the spectroscopic stellar parameters into the error analysis, $T_{\rm eff}$ and [Fe/H] were drawn from Gaussian distributions in the MCMC routine. This method also gives us a more precise estimate for $\log g$ of the primary star. This $\log g$ value was incorporated into the spectral classifications process (Section 3.1) to better constrain the $T_{\rm eff}$, [Fe/H] and $v \sin i_{\rm rot}$ estimates.

3.3.2 Spin–orbit synchronization

For stellar mass binaries at short periods, spin–orbit synchronization via tidal interactions is expected to occur within ∼100 myr (Zahn 1977; Hut 1981). If we assume spin–orbit synchronization for these systems and that the stellar spin-axis is near perpendicular to our line of sight ($i_{\rm orb} = i_{\rm rot}$), then it is also possible to derive model-independent estimates of the stellar masses and radii (e.g. Beatty et al. 2007). The masses and radii of components A and B can be calculated from purely observable quantities using

$$M_1 = \frac{P}{2\pi G}\left(\frac{a}{R_1}\right)^2 (v \sin i_{\rm rot})^2 \times \left[\frac{(a/R_1) v \sin i_{\rm rot} - K\sqrt{1-e^2}}{\sin^3 i_{\rm orb}}\right] \quad (2)$$

$$M_2 = \frac{P}{2\pi G}\left(\frac{a}{R_1}\right)^2 \left[\frac{K(v \sin i_{\rm rot})^2\sqrt{1-e^2}}{\sin^3 i_{\rm orb}}\right] \quad (3)$$

$$R_1 = \frac{P}{2\pi}\frac{v \sin i_{\rm rot}}{\sin i_{\rm orb}} \quad (4)$$

$$R_2 = R_1\left(\frac{R_2}{R_1}\right). \quad (5)$$

We caution that spin–orbit synchronization and the alignment of the stellar spin-axis should not be automatically assumed. Although rapid synchronization is expected for binary systems, some previous F-M binaries have been measured to be asynchronous (e.g. Pont et al. 2005, 2006; Triaud et al. 2013). In addition, whilst the alignment of the stellar spin and companion orbital axes is also often predicted from formation and tidal interactions (and by extension of the transit geometry the stellar spin-axis should also be perpendicular to our line of sight) spin–orbit misaligned stellar binaries have been identified (DI Her, KOI-368; Albrecht et al. 2009; Zhou & Huang 2013). It is therefore necessary to compare the stellar parameter results from synchronization against that of isochrone fitting before this method can be adopted.

For each iteration of the global minimization and MCMC routine, we also calculated the primary and companion masses and radii assuming synchronization. The adopted $v \sin i_{\rm rot}$ value was given by the spectroscopic analysis and was drawn from a Gaussian distribution in the MCMC error analysis.

3.3.3 Combined mass–radius estimate

We also perform a combined analysis, where the mass and radius are calculated using isochrone fitting as described in Section 3.3.1. The expected $v \sin i_{\rm rot}$ is then derived using the period and radius, and compared to the measured $v \sin i_{\rm rot}$. We calculate an additional χ^2 term,

$$\chi^2_{v \sin i_{\rm rot}} = \left(\frac{2\pi R_1 \sin i_{\rm orb}/P - v \sin i_{\rm rot}}{\Delta v \sin i_{\rm rot}}\right)^2, \quad (6)$$

which is added to the χ^2 from the light curve and radial velocity data. Due to the transit geometry, we approximate $\sin i_{\rm orb} \approx 1$ in the calculation. The MCMC minimization is rerun for this combined analysis.

The probability distributions for the mass and radius, measured using the above techniques, are plotted in Fig. 6. We find that the 2σ confidence regions derived using isochrone and synchronization overlap for all the systems. This indicates that the assumption of spin–orbit synchronization, required for the combined analysis (Section 3.3.3), is valid for all systems. The system parameters from the combined analysis is adopted for discussion here onwards. The stellar and system parameters are presented in Table 4.

We also tested the sensitivity of the final results against various assumptions in the methods outlined above. These tests were performed on the HATS550-016 data set. The limb darkening coefficients were set free and allowed to vary within 0.2 of the values from Claret (2000). The resulting system parameters did not deviate from those presented in Table 4, with no significant increase in the uncertainties. To test the dependence of the results on the Yonsei-Yale isochrones, we performed the analysis in Section 3.3.1 using the Dartmouth isochrones (Dotter et al. 2008) but found no deviation in the results. To test the effectiveness of reconstructive TFA (Kovács et al. 2005) at recovering the true transit shape, we analysed the HATS550-016 system using only the HATSouth discovery data by excluding the follow-up photometry observations and found no significant deviation in the results; however, the uncertainties were increased by a factor of ∼2–3. We caution that correlated noise, present in the follow-up light curve, were unaccounted for in the analysis and may lead to underestimated uncertainties.

4 DISCUSSION

We have presented the discovery of four transiting VLMSs, with masses ranging from 0.1 to 0.2 $M_\odot$. Their properties are discussed briefly below.

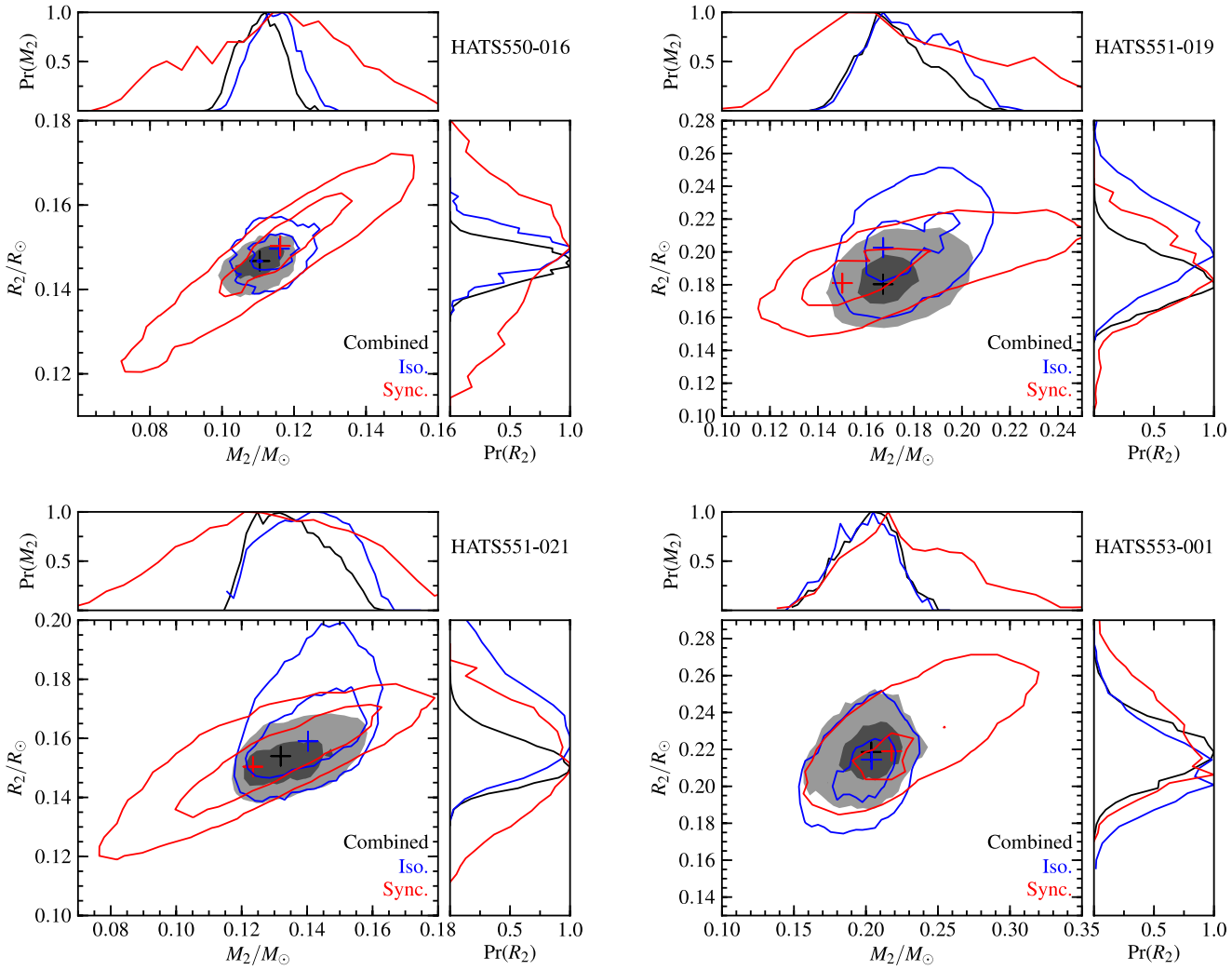

Figure 6. The 1σ and 2σ confidence regions for the masses and radii of the VLMS systems presented in this study. We plot individual confidence regions derived from the isochrone fit (blue), assuming spin–orbit synchronization (red) and the combined analysis (grey). The confidence regions from the combined analysis is adopted. The corresponding crosses mark the peak of the probability distributions.

Table 4. Properties of the HATSouth transiting VLMS systems.

Parameter	HATS550-016	HATS551-019	HATS551-021	HATS553-001
Fitted parameters				
P (d)	$2.051\,811^{+0.000\,002}_{-0.000\,002}$	$4.68681^{+0.000\,02}_{-0.000\,01}$	$3.63637^{+0.000\,05}_{-0.000\,05}$	$3.80405^{+0.000\,01}_{-0.000\,01}$
T_0 (HJD)	$245\,5104.286^{+0.001}_{-0.001}$	$245\,5474.179^{+0.001}_{-0.002}$	$245\,5087.426^{+0.002}_{-0.003}$	$245\,5093.563^{+0.002}_{-0.001}$
$R_{\rm sum}$	$0.196^{+0.003}_{-0.004}$	$0.149^{+0.006}_{-0.008}$	$0.131^{+0.004}_{-0.005}$	$0.158^{+0.005}_{-0.007}$
R_2/R_1	$0.1205^{+0.0003}_{-0.0003}$	$0.107^{+0.002}_{-0.002}$	$0.124^{+0.003}_{-0.002}$	$0.136^{+0.003}_{-0.004}$
i (°)	90^{+1}_{-1}	85^{+1}_{-1}	90^{+1}_{-1}	$83.4^{+0.4}_{-0.3}$
$e\cos\omega$	$-0.001^{+0.003}_{-0.002}$	$-0.003^{+0.002}_{-0.005}$	$0.003^{+0.002}_{-0.002}$	$0.000^{+0.001}_{-0.002}$
$e\sin\omega$	$0.08^{+0.02}_{-0.02}$	$0.04^{+0.02}_{-0.02}$	$0.06^{+0.02}_{-0.02}$	$0.03^{+0.02}_{-0.02}$
K (km s^{-1})	$17.7^{+0.4}_{-0.5}$	$18.4^{+0.6}_{-0.7}$	$16.3^{+0.2}_{-0.2}$	$20.9^{+0.8}_{-0.9}$
Derived parameters				
$\log g$	$4.25^{+0.02}_{-0.02}$	$4.01^{+0.05}_{-0.05}$	$4.30^{+0.04}_{-0.04}$	$4.13^{+0.05}_{-0.05}$
Age (Gyr)	5^{+3}_{-1}	6^{+2}_{-2}	4^{+3}_{-4}	3^{+2}_{-2}
M_1 ($M_\odot$)	$0.97^{+0.05}_{-0.06}$	$1.10^{+0.05}_{-0.09}$	$1.1^{+0.1}_{-0.1}$	$1.2^{+0.1}_{-0.1}$
R_1 ($R_\odot$)	$1.22^{+0.02}_{-0.03}$	$1.70^{+0.09}_{-0.09}$	$1.20^{+0.08}_{-0.01}$	$1.58^{+0.08}_{-0.03}$
M_2 ($M_\odot$)	$0.110^{+0.005}_{-0.006}$	$0.17^{+0.01}_{-0.01}$	$0.132^{+0.014}_{-0.005}$	$0.20^{+0.01}_{-0.02}$
R_2 ($R_\odot$)	$0.147^{+0.003}_{-0.004}$	$0.18^{+0.01}_{-0.01}$	$0.154^{+0.006}_{-0.008}$	$0.22^{+0.01}_{-0.01}$

4.1 HATS550-016B

HATS550-016B is the lowest mass star within our sample and is the second lowest mass star known with mass and radius determined to better than 10 per cent (after J1219-39b; Triaud et al. 2013). It has a mass and radius of $0.110^{+0.005}_{-0.006}\,M_\odot$ and $0.147^{+0.003}_{-0.004}\,R_\odot$, and orbits a relatively metal deficient ([Fe/H] $= -0.60 \pm 0.06$) F-type star of age 5^{+3}_{-1} Gyr in a period of $2.051\,811^{+0.000\,002}_{-0.000\,002}$ d. The radius of HATS550-016B is inflated by 13 per cent compared to Baraffe et al. (1998) models, assuming that it has the same metallicity as the primary star. It is the only star in this sample that is inflated with respect to the isochrones.

4.2 HATS551-019B

HATS551-019B is a $0.17^{+0.01}_{-0.01}\,M_\odot$, $0.18^{+0.01}_{-0.01}\,R_\odot$ VLMS with a $4.686\,81^{+0.000\,02}_{-0.000\,01}$ d period orbit about a 6^{+2}_{-2} Gyr F subgiant, with a subsolar metallicity of [Fe/H] $= -0.4 \pm 0.1$. Since the follow-up photometry of HATS551-019 covers only the egress event, the HATSouth discovery light curves, detrended using simultaneous TFA, are also used to constrain the R_2/R_1 ratio. The radius of HATS551-019B agrees with theoretical predictions to within errors.

4.3 HATS551-021B

HATS551-021B is a $0.132^{+0.014}_{-0.005}\,M_\odot$, $0.154^{+0.006}_{-0.008}\,R_\odot$ VLMS in a $3.636\,37^{+0.000\,05}_{-0.000\,05}$ d period orbit about an F dwarf with a metallicity of [Fe/H] $= -0.4 \pm 0.1$. The age of the primary star is ill defined from isochrone fitting (4^{+3}_{-4} Gyr). We find no chromospheric Ca H&K emission nor excess Li absorption, indicating that the system is likely >1 Gyr in age. No follow-up photometry is available for HATS551-021, so the R_2/R_1 ratio is constrained purely from HATSouth discovery light curves. The radius of HATS551-021B matches theoretical isochrones very well.

4.4 HATS553-001B

HATS553-001B is a VLMS with mass of $0.20^{+0.01}_{-0.02}\,M_\odot$, and radius of $0.22^{+0.01}_{-0.01}\,R_\odot$, orbiting a 3^{+2}_{-2} Gyr F-type star of near solar metallicity ([Fe/H] $= -0.1 \pm 0.2$) in a $3.804\,05^{+0.000\,01}_{-0.000\,01}$ d period orbit. The radius of HATS553-001B matches the isochrones to within errors.

4.5 Mass–radius relationship

The masses and radii of the VLMS companions presented in this paper, as well as that of known well-studied VLMSs (Table 5), are plotted in Fig. 7. Of the VLMSs reported in this study, we find only HATS550-016B to be inflated compared to theoretical isochrones; HATS551-019B, HATS551-021B and HATS553-001B, agree with the isochrone mass–radius relations to within measurement uncertainties.

Table 5. Properties of known VLMSs[a].

Object	Mass ($M_\odot$)	Radius ($R_\odot$)	Method	[Fe/H]	Period (d)	$T_{\rm eff}$ (K)	Companion $T_{\rm eff}$ (K)	Reference
F, G-M Binaries[b]								
HAT-TR-205-013B	0.124 ± 0.01	0.167 ± 0.006	SB1, synchronization[c]	0.0 ± 0.5	2.23		6295 ± 200	Beatty et al. (2007)
J1219-39B	0.091 ± 0.002	$0.1174^{+0.0071}_{-0.0050}$	SB1, isochrone[d]	-0.209 ± 0.072	6.76		5400 ± 90	Triaud et al. (2013)
KIC 1571511B	$0.141\,36^{+0.0051}_{-0.0042}$	$0.17831^{+0.0013}_{-0.0016}$	SB1, isochrone	0.37 ± 0.08	14.02	4090 ± 60	6195 ± 50	Ofir et al. (2012)
T-Lyr0-08070B	0.240 ± 0.019	0.265 ± 0.010	SB1, synchronization	-0.5^e	1.18		6250 ± 140	Fernandez et al. (2009)
T-Lyr1-01662B	0.198 ± 0.012	0.238 ± 0.007	SB1, synchronization	-0.5^e	4.23		6200 ± 30	Fernandez et al. (2009)
K, M-M Binaries								
CM Dra A	0.2130 ± 0.0009	0.2534 ± 0.0019	SB2[f]	-0.3 ± 0.12	1.27	3130 ± 70	3120 ± 70	Morales et al. (2009) Terrien et al. (2012)
CM Dra B	0.2141 ± 0.0010	0.2396 ± 0.0015	SB2	-0.3 ± 0.12	1.27	3120 ± 70	3130 ± 70	Morales et al. (2009) Terrien et al. (2012)
Kepler-16B	$0.202\,55^{+0.000\,66}_{-0.000\,65}$	$0.226\,23^{+0.000\,59}_{-0.000\,53}$	SB1, photodynamical[g]	-0.3 ± 0.2	41.08		4450 ± 150	Doyle et al. (2011)
KOI-126B	0.2413 ± 0.003	0.2543 ± 0.0014	SB1, photodynamical	0.15 ± 0.08	1.77 (About KOI-126C) 33.92 (About KOI-126A)		5875 ± 100 (KOI-126A)	Carter et al. (2011)
KOI-126C	0.2127 ± 0.0026	0.2318 ± 0.0013	SB1, photodynamical	0.15 ± 0.08	1.77 (About KOI-126B) 33.92 (About KOI-126A)		5875 ± 100 (KOI-126A)	Carter et al. (2011)
Single Stars								
GJ 191	0.281 ± 0.014	0.291 ± 0.025	Interferometry	-0.99 ± 0.04		3570 ± 160		Ségransan et al. (2003) Woolf & Wallerstein (2005)
GJ 551	0.123 ± 0.006	0.141 ± 0.007	Interferometry	0.21 ± 0.03^h		3098 ± 56		Ségransan et al. (2003) Valenti & Fischer (2005) Demory et al. (2009)
GJ 699	0.146 ± 0.015	0.1867 ± 0.0012	Interferometry	-0.39 ± 0.17		3224 ± 10		Boyajian et al. (2012) Rojas-Ayala et al. (2012)

[a] With $0.08 < M < 0.3\,M_\odot$, mass and radius measured to better than 10 per cent precision and valid [Fe/H] measurements.
[b] Assume primary star [Fe/H].
[c] SB1, synchronization: single-lined stellar binary, parameters derived from assuming spin–orbit synchronization.
[d] SB1, isochrone: single-lined stellar binary, parameters derived from isochrone fitting.
[e] [Fe/H] adopted from table 13 of Fernandez et al. (2009), by finding the best-matching results between the isochrone and synchronization techniques. We assume an error of 0.5 dex (grid size) in our analysis of BIC and F-test.
[f] SB2: double-lined eclipsing binary, parameters determined dynamically.
[g] SB1, photodynamical: global analysis of single-lined radial velocity data and light-curve transit timing variations for multibody systems.
[h] Adopting [Fe/H] of α Centauri A, see Johnson & Apps (2009).

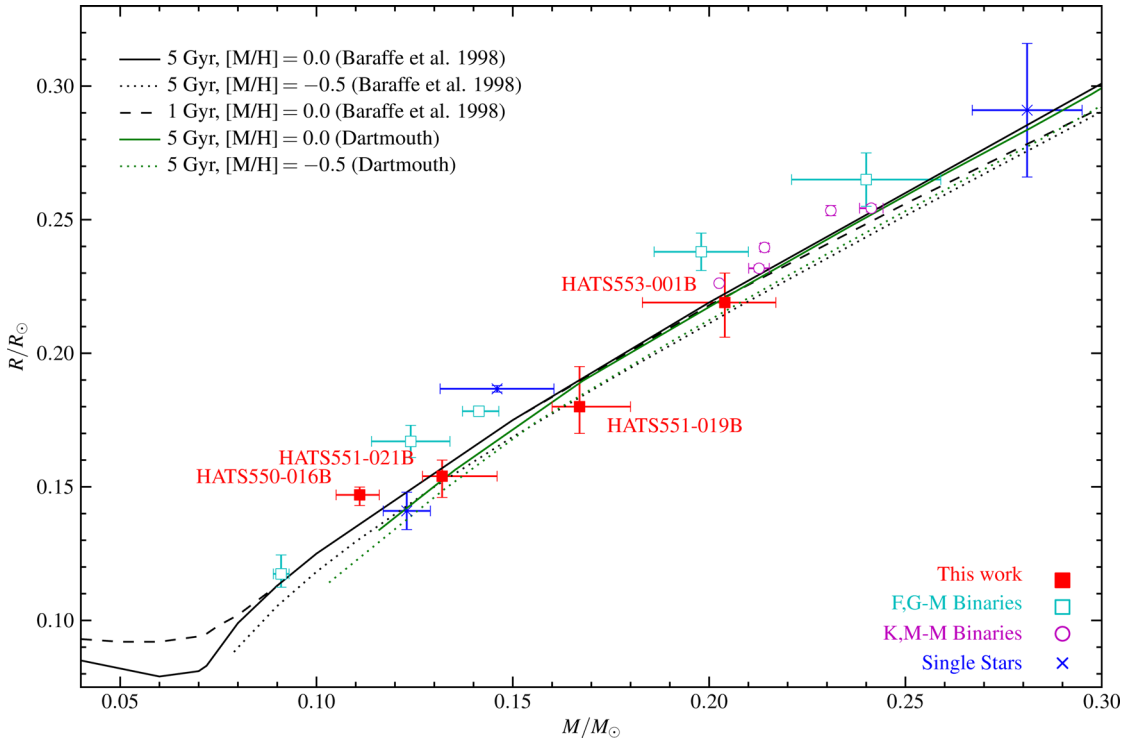

Figure 7. Mass–radius diagram of the VLMSs. New VLMSs presented in this paper are plotted in red and labelled, known F,G-M eclipsing binaries are plotted as cyan squares, M-M eclipsing binaries as magenta circles and single stars measured by interferometry as blue crosses (Table 5). The isochrone lines from Baraffe et al. (1998) at 1.0 Gyr solar (black dashed), 5.0 Gyr solar (black solid), 5.0 Gyr [M/H] = −0.5 (black dotted), and from Dotter et al. (2008) at 5.0 Gyr solar (green solid), 5.0 Gyr [M/H] = −0.5 (green dotted) are marked. The corresponding 1 and 5 Gyr isochrones for brown dwarfs from Baraffe et al. (2003) are plotted in black, but not used in further analysis.

We tested for any general radius deviation between the observed VLMS population and the isochrones. The theoretical radii are taken from the 5 Gyr isochrones from Baraffe et al. (1998), interpolated between [M/H] = −0.5 and 0.0, and linearly extrapolated beyond when necessary, to account for the metallicity dependence. For each object, we sample the isochrones via a Monte Carlo analysis, drawing mass and metallicity values from Gaussian distributions about the measured values and their associated uncertainties, and derive a predicted model radius and uncertainty. For this discussion on the radius deviation between model and measurements, we adopted the radius uncertainty as the quadrature addition of the uncertainties in the measurement and model sampling.

We also note that the difference between the Baraffe et al. (1998) and the Dartmouth isochrones (Dotter et al. 2008) is minor compared to the deviation from observations (see green isochrone lines in Fig. 7); hence, the following calculations were performed relative to the Baraffe et al. (1998) isochrones only. In addition, we also explored isochrones of younger ages and shorter mixing length using the Baraffe et al. (1998) isochrones; neither factors have obvious effects at this mass range.

The χ^2 of the observed population is compared to (Model A) the isochrones without modification and (Model B) with isochrone radii inflated by 1.05. If the χ^2 is calculated with the measurement uncertainties taken at face value, the Bayesean information criterion (BIC) between the two models is 50 (χ^2/dof = 7 and 3, for Models A and B, respectively), tentatively favouring an inflation of radius from the isochrones. The F-test for the variance ratio of the fit to the two models gives a p-value of 0.08, suggesting a very tentative preference towards Model B. Both BIC and the F-test account for the greater complexity of Model B over A. A number of studies (Morales et al. 2010; Windmiller, Orosz & Etzel 2010; Feiden & Chaboyer 2012) have commented that the presence of spots can impose radii uncertainties of the order of 2 per cent in these measurements. After imposing a minimum radius uncertainty of 2 per cent on the same population, we find BIC = 21 (χ^2/dof = 3 and 2, for Models A and B, respectively) and F-test p-value of 0.11. The F-test result, after inflating the uncertainties, suggests no real preference between Models A and B. In addition, 5 per cent systematic deviation between measurements and model is significantly smaller than the ∼10 per cent stated by earlier studies (e.g. Ribas 2006) and agrees with more recent studies of higher mass double-lined M-dwarf binaries, using newer isochrone sets (e.g. Kraus et al. 2011; Feiden & Chaboyer 2012; Spada et al. 2013).

The rms scatter of observed − theoretical stellar radius difference (3 per cent) is slightly larger than the mean observational uncertainties (5 per cent). Whilst this is likely due to the underestimated observational uncertainties, it may also point towards secondary factors, beyond mass and metallicity, that affect the radii of VLMSs. Fig. 8 plots the radius discrepancy against mass, orbital period and incident flux from the primary star. For each factor, the Pearson correlation coefficient r is calculated, weighted by the measurement uncertainties, with the radius uncertainties of M-M binaries increased to 2 per cent. We find no significant correlation with any of these parameters.

In particular, activity-induced inflation of the stellar radius should be correlated with shorter period if faster rotation gives rise to more powerful internal dynamos (López-Morales 2007). This is not observed in the low-mass population. However, it is not obvious that we expect such period–activity–radius dependences, since the dynamos in fully convective stars may operate differently to

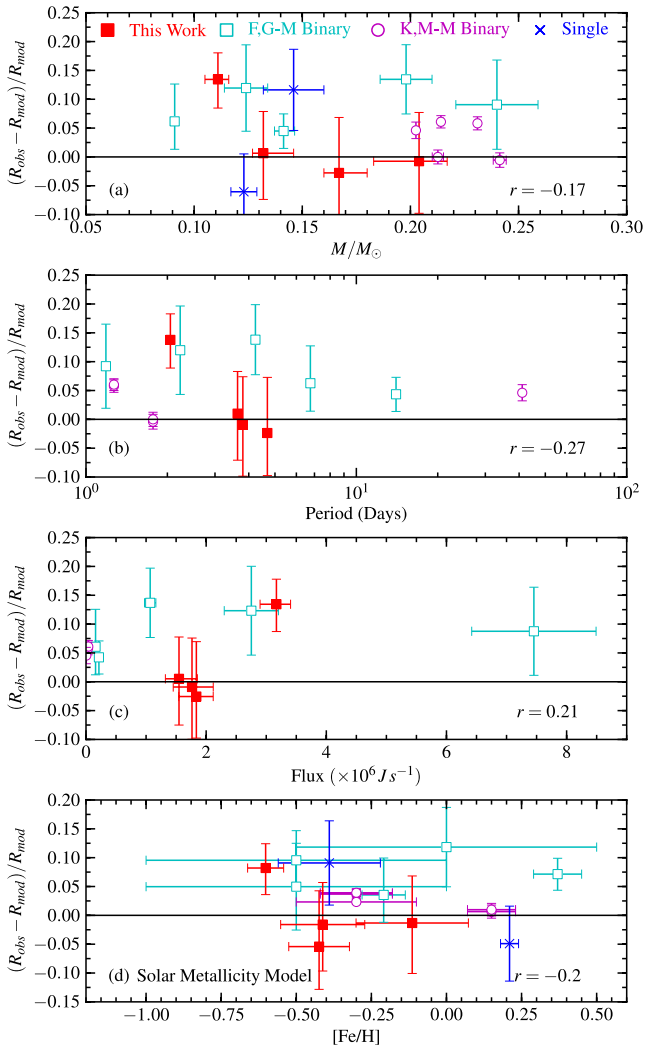

Figure 8. The observed − theoretical radius difference of the VLMSs are plotted against their (a) mass, (b) system period and (c) incident flux from the primary star. The theoretical radius is derived from the Baraffe et al. (1998) isochrones, interpolated to the [Fe/H] of each system. The objects without relevant orbital period and host star flux are omitted where necessary. Panel (d) shows the radius deviation to a solar metallicity isochrone as a function of the measured metallicity. The Pearson correlation coefficient r is calculated for each panel. We find no significant correlation between the radius discrepancy and any of these parameters.

solar-type stars (Chabrier & Küker 2006). In addition, the paucity of well-studied VLMS binaries in >10 d periods prevents us from drawing strong conclusions regarding the period–radius dependence. We also note the minimal dependence between incident flux and radius deviation. The influence of irradiation and disequilibrium chemistry on exoplanets has been contemplated (e.g. Knutson, Howard & Isaacson 2010); similar mechanisms that alter the top-level opacity of VLMSs may be possible, but clearly are not significant. In addition, whilst external influences are often considered when discussing the radius discrepancy of binary systems, we note that field M-dwarfs measured via interferometry have shown an equivalent radius discrepancy to the models (e.g. Berger et al. 2006; Boyajian et al. 2012; Spada et al. 2013) and that there is no necessary expectation for radius, period and incident flux to be correlated.

Metallicity has previously been suggested as a cause in the radius discrepancy (e.g. Berger et al. 2006; Burrows, Heng & Nampaisarn 2011). Fig. 8 also plots the radius deviation to the solar metallicity isochrone. We find no correlation between the measured metallicity and the radius deviation. The lack of dependence on metallicity for VLMSs agrees with the analysis by Spada et al. (2013), who suggest that metallicity is only weakly correlated with radius, but more strongly affects luminosity and effective temperature.

ACKNOWLEDGEMENTS

Development of the HATSouth project was funded by NSF MRI grant NSF/AST-0723074, operations are supported by NASA grant NNX09AB29G and follow-up observations receive partial support from grant NSF/AST-1108686. Work at the Australian National University is supported by ARC Laureate Fellowship Grant FL0992131. Follow-up observations with the ESO 2.2 m/FEROS instrument were performed under MPI guaranteed time [P087.A-9014(A), P088.A-9008(A), P089.A-9008(A)]. AJ acknowledges support from FONDECYT project 1130857, BASAL CATA PFB-06 and the Millenium Science Initiative, Chilean Ministry of Economy (Nuclei: P10-022-F, P07-021-F). RB and NE are supported by CONICYT-PCHA/Doctorado Nacional and MR is supported by FONDECYT postdoctoral fellowship 3120097. This work is based on observations made with ESO telescopes at the La Silla Observatory under programme IDs P087.A-9014(A), P088.A-9008(A), P089.A-9008(A), P087.C-0508(A) and 089.A-9006(A), and this paper also uses observations obtained with facilities of the Las Cumbres Observatory Global Telescope. We acknowledge the use of the AAVSO Photometric All-Sky Survey (APASS), funded by the Robert Martin Ayers Sciences Fund, and the SIMBAD data base, operated at CDS, Strasbourg, France. Operations at the MPG/ESO 2.2 m telescope are jointly performed by the Max Planck Gesellschaft and the European Southern Observatory. The imaging system GROND has been built by the high-energy group of MPE in collaboration with the LSW Tautenburg and ESO (Greiner et al. 2008). We thank Timo Anguita and Régis Lachaume for their technical assistance during the observations at the MPG/ESO 2.2 m telescope.

REFERENCES

Albrecht S., Reffert S., Snellen I. A. G., Winn J. N., 2009, Nature, 461, 373
Bakos G. Á. et al., 2007, ApJ, 670, 826
Bakos G. Á. et al., 2013, PASP, 125, 154
Baraffe I., Chabrier G., Allard F., Hauschildt P. H., 1998, A&A, 337, 403
Baraffe I., Chabrier G., Barman T. S., Allard F., Hauschildt P. H., 2003, A&A, 402, 701
Bayliss D. et al., 2013, AJ, 146, 113
Beatty T. G. et al., 2007, ApJ, 663, 573
Berger D. H. et al., 2006, ApJ, 644, 475
Bertin E., Arnouts S., 1996, A&AS, 117, 393
Boyajian T. S. et al., 2012, ApJ, 757, 112
Burrows A., Heng K., Nampaisarn T., 2011, ApJ, 736, 47
Carter J. A. et al., 2011, Science, 331, 562
Castelli F., Kurucz R. L., 2004, Astrophysics, preprint (astro-ph/0405087)
Chabrier G., Baraffe I., 2000, ARA&A, 38, 337
Chabrier G., Küker M., 2006, A&A, 446, 1027
Chabrier G., Gallardo J., Baraffe I., 2007, A&A, 472, L17
Claret A., 2000, A&A, 363, 1081
Demory B.-O. et al., 2009, A&A, 505, 205
Dopita M., Hart J., McGregor P., Oates P., Bloxham G., Jones D., 2007, Ap&SS, 310, 255

Dotter A., Chaboyer B., Jevremović D., Kostov V., Baron E., Ferguson J. W., 2008, ApJS, 178, 89
Doyle L. R. et al., 2011, Science, 333, 1602
Feiden G. A., Chaboyer B., 2012, ApJ, 757, 42
Fernandez J. M. et al., 2009, ApJ, 701, 764
Foreman-Mackey D., Hogg D. W., Lang D., Goodman J., 2013, PASP, 125, 306
Gray R. O., Corbally C. J., 1994, AJ, 107, 742
Greiner J. et al., 2008, PASP, 120, 405
Gustafsson B., Edvardsson B., Eriksson K., Jørgensen U. G., Nordlund Å., Plez B., 2008, A&A, 486, 951
Hellier C. et al., 2012, MNRAS, 426, 739
Husser T.-O., Wende-von Berg S., Dreizler S., Homeier D., Reiners A., Barman T., Hauschildt P. H., 2013, A&A, 553, A6
Hut P., 1981, A&A, 99, 126
Irwin J. M. et al., 2011, ApJ, 742, 123
Johnson J. A., Apps K., 2009, ApJ, 699, 933
Kaufer A., Pasquini L., 1998, in D'Odorico S., ed., SPIE Conf. Ser., Vol. 3355, Optical Astronomical Instrumentation. SPIE, Bellingham, p. 844
Knutson H. A., Howard A. W., Isaacson H., 2010, ApJ, 720, 1569
Kovács G., Zucker S., Mazeh T., 2002, A&A, 391, 369
Kovács G., Bakos G., Noyes R. W., 2005, MNRAS, 356, 557
Kraus A. L., Tucker R. A., Thompson M. I., Craine E. R., Hillenbrand L. A., 2011, ApJ, 728, 48
Kroupa P., 2001, MNRAS, 322, 231
Laughlin G., Crismani M., Adams F. C., 2011, ApJ, 729, L7
López-Morales M., 2007, ApJ, 660, 732
López-Morales M., Ribas I., 2005, ApJ, 631, 1120
Metcalfe T. S., Mathieu R. D., Latham D. W., Torres G., 1996, ApJ, 456, 356
Mohler-Fischer M. et al., 2013, A&A, 558, A55
Morales J. C. et al., 2009, ApJ, 691, 1400
Morales J. C., Gallardo J., Ribas I., Jordi C., Baraffe I., Chabrier G., 2010, ApJ, 718, 502
Nefs S. V. et al., 2013, MNRAS, 431, 3240
Nelson B., Davis W. D., 1972, ApJ, 174, 617
Ofir A., Gandolfi D., Buchhave L., Lacy C. H. S., Hatzes A. P., Fridlund M., 2012, MNRAS, 423, L1
Penev K. et al., 2013, AJ, 145, 5
Pont F., Melo C. H. F., Bouchy F., Udry S., Queloz D., Mayor M., Santos N. C., 2005, A&A, 433, L21
Pont F. et al., 2006, A&A, 447, 1035
Popper D. M., Etzel P. B., 1981, AJ, 86, 102
Queloz D. et al., 2000, A&A, 354, 99
Ribas I., 2006, Ap&SS, 304, 89
Rojas-Ayala B., Covey K. R., Muirhead P. S., Lloyd J. P., 2012, ApJ, 748, 93
Ségransan D., Kervella P., Forveille T., Queloz D., 2003, A&A, 397, L5
Simon M., Schaefer G. H., Prato L., Ruíz-Rodríguez D., Karnath N., Franz O. G., Wasserman L. H., 2013, ApJ, 773, 28
Smalley B. et al., 2012, A&A, 547, A61
Southworth J., Maxted P. F. L., Smalley B., 2004, MNRAS, 351, 1277
Sozzetti A., Torres G., Charbonneau D., Latham D. W., Holman M. J., Winn J. N., Laird J. B., O'Donovan F. T., 2007, ApJ, 664, 1190
Spada F., Demarque P., Kim Y.-C., Sills A., 2013, ApJ, 776, 87
Swift D. C. et al., 2012, ApJ, 744, 59
Terrien R. C., Fleming S. W., Mahadevan S., Deshpande R., Feiden G. A., Bender C. F., Ramsey L. W., 2012, ApJ, 760, L9
Torres G., Ribas I., 2002, ApJ, 567, 1140
Torres G., Andersen J., Giménez A., 2010, A&AR, 18, 67
Triaud A. H. M. J. et al., 2013, A&A, 549, A18
Valenti J. A., Fischer D. A., 2005, ApJS, 159, 141
Windmiller G., Orosz J. A., Etzel P. B., 2010, ApJ, 712, 1003
Woolf V. M., Wallerstein G., 2005, MNRAS, 356, 963
Yi S., Demarque P., Kim Y.-C., Lee Y.-W., Ree C. H., Lejeune T., Barnes S., 2001, ApJS, 136, 417
Zahn J.-P., 1977, A&A, 57, 383
Zhou G., Huang C. X., 2013, ApJ, 776, L35

APPENDIX A: LIGHT-CURVE AND RADIAL VELOCITY DATA

Tables A1–A4 present the discovery and follow-up light-curve data for the objects presented in this study. Tables A5–A8 present the associated radial velocity data.

Table A1. Differential photometry for HATS550-016.

BJD-240 0000	Flux	ΔFlux	Instrument	Filter
551 03.463 354	0.987 94	0.010 25	HS	r'
551 03.479 516	1.002 49	0.010 28	HS	r'
551 03.485 975	1.022 98	0.009 73	HS	r'
551 04.721 430	0.991 44	0.007 34	HS	r'
551 30.407 508	0.992 68	0.008 48	HS	r'

This table is available in a machine-readable form in the online journal. A portion is shown here for guidance regarding its form and content.

Table A2. Differential photometry for HATS551-019.

BJD-240 0000	Flux	ΔFlux	Instrument	Filter
550 83.758 920	1.002 76	0.003 11	HS	r'
550 83.762 160	1.000 41	0.003 05	HS	r'
550 83.765 520	1.002 70	0.003 03	HS	r'
550 83.768 730	0.995 39	0.002 98	HS	r'
550 83.772 100	1.002 67	0.002 96	HS	r'

This table is available in a machine-readable form in the online journal. A portion is shown here for guidance regarding its form and content.

Table A3. Differential photometry for HATS551-021.

BJD-240 0000	Flux	ΔFlux	Instrument	Filter
550 83.758 920	0.979 41	0.005 66	HS	r'
550 83.762 160	0.992 82	0.005 77	HS	r'
550 83.765 520	0.978 66	0.005 72	HS	r'
550 83.768 730	0.980 86	0.005 69	HS	r'
550 83.772 100	0.982 39	0.005 83	HS	r'

This table is available in a machine-readable form in the online journal. A portion is shown here for guidance regarding its form and content.

Table A4. Differential photometry for HATS553-001.

BJD-240 0000	Flux	ΔFlux	Instrument	Filter
550 91.519 969	0.986 37	0.005 68	HS	r'
550 91.523 285	0.990 27	0.005 33	HS	r'
550 91.526 738	0.995 89	0.005 28	HS	r'
550 91.530 049	0.994 46	0.005 22	HS	r'
550 91.533 508	0.986 95	0.005 12	HS	r'

This table is available in a machine-readable form in the online journal. A portion is shown here for guidance regarding its form and content.

Table A5. Radial velocities for HATS550-016.

BJD-240 0000	RV (km s^{-1})	ΔRV (km s^{-1})	Instrument
561 64.877 923	21.49	0.08	CORALIE
562 37.817 487	5.81	0.08	CORALIE
562 38.819 306	16.33	0.08	CORALIE
562 39.850 619	6.69	0.08	CORALIE
562 41.679 708	−3.25	0.08	CORALIE

This table is available in a machine-readable form in the online journal. A portion is shown here for guidance regarding its form and content.

Table A6. Radial velocities for HATS551-019.

BJD-240 0000	RV (km s^{-1})	ΔRV (km s^{-1})	Instrument
554 97.745 634	10.14	0.04	CORALIE
556 08.701 137	33.44	0.04	CORALIE
556 10.699 243	−0.51	0.05	CORALIE
563 74.907 520	−7.46	0.61	ANU2.3 m/ECHELLE
563 75.887 520	4.32	0.56	ANU2.3 m/ECHELLE

This table is available in a machine-readable form in the online journal. A portion is shown here for guidance regarding its form and content.

Table A7. Radial velocities for HATS551-021.

BJD-240 0000	RV (km s^{-1})	ΔRV (km s^{-1})	Instrument
554 97.766 487	28.16	0.06	CORALIE
556 08.553 710	−1.30	0.07	CORALIE
556 10.627 251	26.18	0.06	CORALIE
558 13.836 900	28.69	0.28	FEROS
558 14.854 700	8.32	0.25	FEROS

This table is available in a machine-readable form in the online journal. A portion is shown here for guidance regarding its form and content.

Table A8. Radial velocities for HATS553-001.

BJD-240 0000	RV (km s^{-1})	ΔRV (km s^{-1})	Instrument
563 74.955 480	26.75	0.80	ANU2.3 m/ECHELLE
563 75.925 980	−3.30	0.71	ANU2.3 m/ECHELLE
563 77.923 100	25.50	0.74	ANU2.3 m/ECHELLE
563 78.918 650	23.46	0.73	ANU2.3 m/ECHELLE
563 80.938 390	−2.56	1.24	ANU2.3 m/ECHELLE

This table is available in a machine-readable form in the online journal. A portion is shown here for guidance regarding its form and content.

SUPPORTING INFORMATION

Additional Supporting Information may be found in the online version of this article:

Table A1. Differential photometry for HATS550-016.
Table A2. Differential photometry for HATS551-019.
Table A3. Differential photometry for HATS551-021.
Table A4. Differential photometry for HATS553-001.
Table A5. Radial velocities for HATS550-016.
Table A6. Radial velocities for HATS551-019.
Table A7. Radial velocities for HATS551-021.
Table A8. Radial velocities for HATS553-001 (http://mnras.oxfordjournals.org/lookup/suppl/doi:10.1093/mnras/stt2100/-/DC1).

Please note: Oxford University Press are not responsible for the content or functionality of any supporting materials supplied by the authors. Any queries (other than missing material) should be directed to the corresponding author for the article.

This paper has been typeset from a TEX/LATEX file prepared by the author.